$E \times B$ advection of trace ions in tokamak microturbulence

T. Hauff and F. Jenko

Max-Planck-Institut für Plasmaphysik,

EURATOM Association, 85748 Garching, Germany

Abstract

The $E \times B$ advection of trace ions in realistic tokamak microturbulence (as described by nonlinear gyrokinetics) is investigated. In order to understand the consequences of effects like large gyroradii, fluctuation anisotropies, zonal flows, or poloidal drifts, they are first studied in the framework of a model which is based on self-created stochastic potentials. Direct numerical simulations are performed, and a semi-analytical model is presented which provides qualitative as well as quantitative insight into the nature of passive tracer transport. One finds that the resulting diffusivities may be larger than expected as long as the gyroradii do not exceed the turbulence correlation length(s) and the poloidal drift velocities are sufficiently small.

I. INTRODUCTION

One of the key goals of magnetic fusion research is to understand, predict, and control the turbulent transport of particles, momentum, and energy across flux surfaces. In this context, one is also interested in the behavior of passive tracers in prescribed turbulent fields – mainly for two reasons. First, if the concentration of a given particle/ion species is quite low (as it often is for impurities, α particles, or beam ions), the back-reaction on the turbulence may be neglected and the "passive tracer" description is thus justified. And second, this approximation makes the complex problem of plasma turbulence somewhat more accessible, allowing for the construction of tractable models which may provide both qualitative and quantitative insight.

In the present paper, we will consider the $E \times B$ advection of trace ions from a rather fundamental point of view. To this aim, we restrict our study to the dynamics of passive tracers in a given perpendicular plane (see, e.g., Ref. [1], Ch. 14, and references therein), leaving questions related to parallel dynamics (Ref. [1], Ch. 15) and the transition to an active tracer description [2–5] for future work. It will turn out that the relative simplicity of this system enables us to obtain qualitative insight into a number of fundamental mechanisms governing transport in turbulent plasmas which would be much harder to extract from more complex models (where it is usually impossible to discriminate between various co-existing effects). Moreover, our approach even allows us to derive quantitative expressions for the resulting particle diffusivities. Many of these findings are expected to carry over to more general models, either directly or by analogy.

In this spirit, we will assess the role of effects like large gyroradii [6–9], fluctuation anisotropies [10], zonal flows [11], or poloidal drifts [8]. Although there exists a significant number of studies addressing their influence on transport, there is currently no coherent picture concerning most of them. This is true, in particular, for the effect of large gyroradii on test particle transport. Here, several previously published results seem to contradict each other, often because "special" realizations of turbulent fields were used. It is therefore a key aim of this study to provide a systematic approach to these phenomena, allowing to reconcile some of the observed differences in the literature. Also, the strong influence of homogeneous poloidal drifts on the radial transport of tracers is reported and assessed in this paper for the first time (to our knowledge). To begin with, we will study the behavior

of tracers in self-created stochastic potentials. Direct numerical simulations are performed, and a semi-analytical model (based on the work in Ref. [9]) is presented which is able to capture the main effects quite accurately. Based on these preparatory investigations, we will then analyze the particle dynamics in realistic turbulent fields as described by nonlinear gyrokinetics.[12] Here, the point is to identify the physical processes controlling the turbulent transport of trace ions in magnetized plasmas, and to characterize their interplay.

The structure of the present paper is as follows. In Sec. II, we provide some basic information about the concepts and definitions underlying this work. In Sec. III, some key results concerning tracers in isotropic stochastic potentials are briefly reviewed. This is mainly done for later reference. In Secs. IV, V, and VI, we then deal in detail with fluctuation anisotropies, zonal flows, and poloidal drift effects, respectively. This is all done in the context of self-created stochastic potentials, in order to be able to isolate and focus on individual effects in a convenient way. In Sec. VII, we then discuss the particle diffusion in realistic turbulent potentials as described by nonlinear gyrokinetics. Finally, in Sec. VIII, we provide a summary along with some conclusions.

II. GENERAL REMARKS

Throughout this paper, we consider the $E \times B$ advection of ions as passive tracers in a plane perpendicular to the background magnetic field, where the corresponding spatial coordinates will be denoted as $\mathbf{x} = (x_1, x_2) = (x, y)$. The fluctuating electrostatic potentials $\phi(\mathbf{x}, t)$ will either be taken from simulations with the gyrokinetic turbulence code GENE [13, 14] or they will be self-created by superposing a sufficiently large number of random harmonic waves:

$$\phi(\mathbf{x}, t) = \sum_{i=1}^{N} A_i \sin(\mathbf{k}_i \cdot \mathbf{x} + \omega_i t + \varphi_i) \,. \tag{1}$$

We define the spatiotemporal autocorrelation function of a potential $\phi(\mathbf{x}, t)$ as

$$E(\mathbf{x}, t) = \langle \phi(0,0)\phi(\mathbf{x}, t) \rangle = \lim_{L\to\infty} \lim_{T\to\infty} \frac{\int_{-L}^{L}\int_{-L}^{L}\int_{-T}^{T} \phi(\mathbf{x}', t')\phi(\mathbf{x}' + \mathbf{x}, t' + t) d^2x' dt'}{8L^2T}. \tag{2}$$

Here, the ensemble average has been replaced by a spatiotemporal average. For the potential given in Eq. (1) the autocorrelation function is easily shown to be

$$E(\mathbf{x}, t) = \sum_{i=1}^{N} \frac{A_i^2}{2} \cos(\mathbf{k}_i \cdot \mathbf{x} + \omega_i t) \,, \tag{3}$$

using elementary trigonometric transformations. Neglecting finite gyroradius effects, the motion of passive particles is described by the (normalized) $E \times B$ drift velocity

$$v_{x_1}^{\mathrm{E}} = -\frac{\partial \phi(\mathbf{x}, t)}{\partial x_2}, \qquad v_{x_2}^{\mathrm{E}} = \frac{\partial \phi(\mathbf{x}, t)}{\partial x_1}\,. \tag{4}$$

Finite gyroradius effects are then introduced via the standard gyrokinetic approach, i.e., by averaging the potential over the gyro-orbit of the particle and applying Eq. (4) to this new effective potential.[12] It can be shown that the latter is simply obtained by multiplying each Fourier component of the potential in Eq. (1) with the Bessel function $J_0(k_i \rho)$ (we denote the gyroradius with ρ). Similarly, the respective autocorrelation function is obtained by multiplying each Fourier component in Eq. (3) with $J_0^2(k_i \rho)$.[9]

The transport is quantified in terms of the diffusion coefficient which can be expressed as

$$D_{x_i}(t) \equiv \frac{1}{2}\frac{d}{dt}\langle x_i(t)^2 \rangle\,, \tag{5}$$

where the angular brackets denote ensemble averaging. The number of particles needs to be chosen such that $D(t)$ becomes sufficiently smooth. This number may be minimized via the 'time average' method described in Ref. [15]. Here, intermediate positions of the particles are reinterpreted as starting points of new trajectories.

The equations of motion are solved numerically via a standard fourth-order Runge-Kutta method.[16] For the self-generated potentials, the values of the potential and those of the required derivatives are given analytically for each point in space and time, whereas for the realistic, gyrokinetic potentials they are given as three dimensional arrays, $\phi(x_i, y_j, t_k)$. The values at intermediate space-time positions are then obtained by means of a suitable interpolation scheme.

A key quantity characterizing the potential fluctuations is the Kubo number [17, 18]

$$K \equiv \frac{V \tau_c}{\lambda_c} = \frac{\tau_c}{\tau_{\mathrm{fl}}}\,. \tag{6}$$

Here, τ_c and λ_c denote, respectively, the autocorrelation time and length of the electrostatic potential, V is the mean drift velocity which can be calculated as [18]

$$V = \left(- \left. \frac{\partial^2 E(\mathbf{x}, t)}{\partial x^2} \right|_{\mathbf{x}=t=0} \right)^{1/2}\,, \tag{7}$$

and τ_{fl} is the mean time of flight for a distance of one correlation length. The limits $K \to \infty$ and $K \to 0$ correspond to static and fast fluctuations, respectively. Sometimes, the regime

of $K \lesssim 1$ is labeled 'weak turbulence' or 'quasilinear,' while the $K \gtrsim 1$ regime is called 'strong turbulence' or 'nonlinear.' With the exception of Sec. VII, lengths are normalized with respect to the correlation length of the potential, whereas times are normalized with respect to the inverse gyrofrequency.

The scaling of the diffusion coefficient D with the Kubo number K has been the subject of various previous studies. In the limit of small Kubo numbers, $K \lesssim 1$, the diffusion coefficient is known to scale like $D \propto \lambda_c V K = \tau_c V^2$, whereas in the limit of large Kubo numbers, $K \gtrsim 1$, one has

$$D \propto \lambda_c V K^{\gamma-1} = \lambda_c^{2-\gamma} V^\gamma / \tau_c^{1-\gamma} \tag{8}$$

with $\gamma < 1$ (due to trapping effects).[15, 19] In Ref. [20] (see also the review article [21]), a consideration based on percolation theory suggests $\gamma = 0.7$ for isotropic turbulence – a result which has been confirmed by direct numerical simulations.[9, 15, 19] We note in passing that the small Kubo number result can also be expressed in the form of Eq. (8), setting $\gamma = 2$.

On the basis of these scalings, an analytical approach describing finite gyroradius effects on D has been proposed in Ref. [9]. Here, the quantities V, λ_c, and τ_c, which are inferred from the autocorrelation function $E(\mathbf{x}) = (2\pi)^{-2} \int_{-\infty}^{\infty} d\mathbf{k}\, e^{i\mathbf{k}\cdot\mathbf{x}} E(\mathbf{k})$, are replaced by new values $V^{\rm eff}$, $\lambda_c^{\rm eff}$ and $\tau_c^{\rm eff}$, extracted from the effective autocorrelation function

$$E^{\rm eff}(\mathbf{x}, \rho) = \frac{1}{(2\pi)^2} \int_{-\infty}^{\infty} d\mathbf{k}\, e^{i\mathbf{k}\cdot\mathbf{x}} E(\mathbf{k})\, J_0^2(k\rho)\,. \tag{9}$$

This statistical information can be used together with the above $D(K)$ scalings in the low and high Kubo number regimes (as well as in the transitional regime as we will see in Sec. VII) to derive expressions for the gyroradius dependence of the diffusivity. The formulas obtained this way will be shown to be in good agreement with the results from direct numerical simulations, providing a very intuitive way for understanding finite gyroradius effects. Similar things hold true, e.g., for the effect of fluctuation anisotropies.

III. ISOTROPIC STOCHASTIC POTENTIALS: A BRIEF REVIEW

For completeness and later reference, we would like to begin with a brief review of results for an isotropic Gaussian potential that we have already reported in a previous publication.[9] Here, we created a random potential according to Eq. (1) with $N = 10^5$ and

$A_i = A_{\max} \exp(-k_i^2/8)$. Due to this large number of partial waves, the spatial autocorrelation function was given almost exactly by a Gaussian of the form $E(\mathbf{x}) \propto \exp(-|\mathbf{x}|^2)$. The wave numbers and frequencies were randomly and homogeneously distributed within the intervals $0 \leq |\mathbf{k}_i| \leq k_{\max}$ and $0 \leq \omega_i \leq \omega_{\max}$. The Kubo number was controlled by varying $\omega_{\max}$, i.e., the correlation time. We calculated the diffusion coefficient from direct numerical simulations according to Eq. (5). The result $D(K)$ is plotted for several values of the gyroradius ρ in Fig. 1. For small Kubo numbers, $K \lesssim 1$, the transport is significantly reduced with increasing gyroradius even for $\rho < 1$, whereas for larger Kubo numbers, $K \gtrsim 1$, the transport is practically constant for gyroradii up to the correlation length, and for $\rho > 1$ the reduction is much slower than in the low Kubo number regime.

For the simple case of an isotropic Gaussian autocorrelation function, Eq. (9) can be evaluated analytically as was shown in Ref. [9]. Replacing the Bessel function by its Taylor expansion or by half its envelope for $\rho \lesssim 1$ and $\rho \gtrsim 3$, respectively, we could derive explicit expressions for $E^{\text{eff}}(\mathbf{x}, \rho)$, V^{eff}, λ_c^{eff} (defined here as the e-folding length of E^{eff}), and τ_c^{eff}. Inserting those into the known scaling laws, one obtains a relation between the diffusion coefficient for finite and for vanishing gyroradius:

$$\begin{aligned} D_\rho/D_0 \;\approx\; & 1 + [2 - 3\gamma]\,\rho^2 + \left[\frac{3}{2} - \frac{21}{4}\gamma + \frac{9}{2}\gamma^2\right]\rho^4 \\ & + \left[\frac{1}{2} - \frac{29}{12}\gamma + \frac{27}{4}\gamma^2 - \frac{9}{2}\gamma^3\right]\rho^6 \quad \text{for } \rho \lesssim 1 \end{aligned} \tag{10}$$

and

$$D_\rho/D_0 \approx 1.73^{2-\gamma}\,(4\sqrt{\pi}\rho)^{-\gamma/2} \quad \text{for } \rho \gg 1\,. \tag{11}$$

In Fig. 2, the simulation results for $K = 180$ and $K = 0.18$ are plotted and compared with the corresponding analytical expressions for $\gamma = 0.75$ and $\gamma = 2$ – and the agreement between both approaches is found to be quite good. An extensive discussion of these findings can be found in Ref. [9]. In short, the behavior can be explained as follows. The gyroaveraging process smooths out the potential and therefore reduces the effective drift velocity monotonically with increasing gyroradius. On the other hand, the gyroaveraging increases the correlation length of the potential as can be understood by inspection of Eq. (9). For $\rho \lesssim 1$, the term $J_0(k\rho)$ mainly suppresses the large wavenumber contributions, narrowing the $\mathbf{k}$ spectrum and therefore widening $E(\mathbf{x})$ in real space. For $\rho \gtrsim 1$, the Bessel function tends to reduce the entire spectrum, and it can be shown that the effective correlation length

converges to a fixed value. – For small Kubo numbers, we have $D \propto \tau_c V^2$. Since there is no trapping in that regime, the change of the correlation length is of no relevance, and since $V^{\rm eff}$ is reduced with ρ, D is reduced, too. For large Kubo numbers, trapping dominates the transport, and the correlation length becomes important as we can see in the expression $D \propto \lambda_c^{2-\gamma} V^\gamma / \tau_c^{1-\gamma}$. For $\gamma \approx 0.7$ and $\rho \lesssim 1$, one finds that the reduction of $V^{\rm eff}$ and the increase of $\lambda^{\rm eff}$ balance each other almost perfectly, keeping the diffusion coefficient more or less constant [note that in Eq. (10), both the second-order and the fourth-order term vanish for $\gamma = 2/3$]. Since for $\rho > 1$, the effective correlation length saturates, whereas the effective drift velocity continues to decrease with increasing ρ, the diffusion coefficient is reduced. However, this reduction is slower than for $K < 1$ since the saturated value of $\lambda^{\rm eff}$ is larger than λ_0 (i.e., the correlation length in the zero gyroradius limit) and γ is smaller.

IV. ANISOTROPIC STOCHASTIC POTENTIALS

Now, gyrokinetic simulations show that tokamak microturbulence does not have to be isotropic (see, e.g., Refs. [13, 14]). This calls for a generalization of the ideas developed in the previous section. Consequently, we consider next a spatial autocorrelation function of the form

$$E(\mathbf{x}) \propto e^{-(x/\lambda_x)^2 - (y/\lambda_y)^2} \tag{12}$$

where $\zeta = \lambda_x / \lambda_y$ may deviate from unity. To realize such autocorrelations, we work with $N = 10^3$ partial waves, having checked that $E(\mathbf{x})$ is sufficiently smooth and that the resulting diffusion coefficients are practically unchanged when N is increased.

In a first step, let us consider the limit of vanishing gyroradius. Keeping λ_y (as well as the potential amplitude) fixed and changing only λ_x, one can use $\lambda_I \equiv \lambda_y$ and $V_I = V_x$ as constant reference values denoted by the index I (for *isotropic*). We thus have $\lambda_x = \zeta \lambda_I$ and $V_y = V_I / \zeta$. Inserting these relationships into Eq. (8), we find $D_x = \zeta^{2-\gamma} D_I$ and $D_y = \zeta^{-\gamma} D_I$ with $\gamma = 2$ for $K \lesssim 1$ and $\gamma \approx 0.7$ for $K \gtrsim 1$. Here, D_I is the reference diffusion coefficient obtained for the isotropic case, $\zeta = 1$. In Fig. 3, these four curves are plotted and compared with direct numerical simulations. The isotropic Kubo number $K_I = V_I \tau_c / \lambda_I$ has again been adjusted by varying τ_c, i.e., $\omega_{\rm max}$. The linear regime is represented by simulations performed at $K_I = 0.07$, whereas for the nonlinear regime, $K_I = 70$ was chosen. In this context, we would like to point out that if ζ changes, the 'real' Kubo number changes, too,

but it keeps the same in both directions as long as $E(\mathbf{x})$ is Gaussian ($K_x = K_y = K_I/\zeta$). As can be seen in Fig. 3, the simulation results coincide quite nicely with the analytical predictions. For large Kubo numbers, the diffusion in the x direction is greatly enhanced for $\zeta > 1$. Moreover, invoking mixing length arguments [22], it is reasonable to expect that the fluctuation amplitude is proportional to the radial correlation length, yielding $\phi \propto \zeta$. This leads to $D_x = \zeta^2 D_I$ and $D_y = D_I$, independent of K_I. While this estimate might merely set an upper limit, it is clear that the formation of streamers (radially elongated vortices) implies a significant enhancement of D_x with increasing streamer aspect ratio ζ in a strong turbulence regime.

In a second step, let us now focus on finite gyroradius effects in potentials with given values of K_I and ζ. Our key interest is to find out whether the constant transport regime for $\rho \lesssim 1$ and large K_I (see Fig. 2) is still present or not. In order to apply the scaling approach outlined in the previous section, we have to determine the effective autocorrelation function for Eq. (12) along with the the values of $V^{\rm eff}_{x,y}$ and $\lambda^{\rm eff}_{x,y}$. Unfortunately, in the anisotropic case, the integral in Eq. (9) cannot be solved analytically any more, even if the Bessel function is replaced by appropriate approximations. Thus the analysis has to be done numerically, e.g., using MATHEMATICA. Here, the correlation length is defined as $\lambda^{\rm eff}_x = \sqrt{-2E^{\rm eff}(x)|_{x=0}/\partial_x^2 E^{\rm eff}(x)|_{x=0}}$, which means that we fit a Gaussian to the central region of $E^{\rm eff}(x)$ and determine its width. The resulting D_ρ/D_0 curves are shown in Figs. 4-7. Note that the gyroradius is normalized with respect to λ_y (which is held constant), and that ζ is varied by varying λ_x. The γ values have been determined from simulations with $\rho = 0$ and varying Kubo numbers. In the x direction, γ deviates substantially from the value obtained by Gruzinov and Isichenko ($\gamma = 0.7$) [20, 21]; we find, e.g., that $\gamma = 0.82$ for $\zeta = 4$, which indicates that the trapping effects are weakened with respect to the isotropic case.

In the linear regime ($K \ll 1$), the reduction of D_ρ with increasing ρ is simply a consequence of the reduction of $V^{\rm eff}$. With increasing anisotropy ζ, this reduction is less severe since the influence of gyroaveraging is weaker for larger structures. In the nonlinear regime ($K \gg 1$), we get a more interesting picture. For the x direction, we see that the increasing anisotropy leads to a stronger reduction of the diffusion for small gyroradii. If ρ in Fig. 6 had been normalized with respect to λ_x, this reduction would look even more pronounced. In contrast, for the y direction, we find an increase of D_ρ with increasing anisotropy, and

for $\rho \sim \lambda_y$, the diffusion coefficient becomes even larger than in the zero gyroradius limit. These findings can be explained in terms of the behavior of $\lambda_{x,y}^{\mathrm{eff}}$. For potentials with $\lambda_x > \lambda_y$, the autocorrelation spectrum is more extended in the k_y direction than in the k_x direction. If we now multiply this spectrum with the Bessel function [remember Eq. (9)], it is clear that for small gyroradii ρ the spectrum is damped mainly in the k_y direction. Therefore, λ_y^{eff} increases strongly, whereas λ_x^{eff} stays roughly constant for quite a while. For isotropic turbulence, we find that for $\rho \lesssim 1$, the increase of the effective correlation length balances the reduction of the drift velocity almost exactly in the nonlinear regime. In the anisotropic case, however, this subtle balance is perturbed. While the change in the x correlation length is observed to be too small, the change of its y counterpart is found to be too large.

The fact that the scaling approach outlined above along with its interpretative implications is also applicable to the case of anisotropic fluctuations is demonstrated in Fig. 8. Here, we took a potential with $\zeta = 4$ and performed a number of test particle simulations for a set of different gyroradii for both the linear and the nonlinear regime (precisely speaking, $K = 0.18$ and $K = 180$ have been used). As can be inferred from Fig. 8, the simulation results and the analytical curves are in good agreement, giving evidence that the model still provides important qualitative as well as quantitative insight.

In summary, we can state that the presence of anisotropic, streamer-like structures (as indicated by $\lambda_x > \lambda_y$) tends to enhance the transport in the x direction in the zero gyroradius limit. On the other hand, one finds a stronger reduction of the transport with increasing gyroradius than in the isotropic case. In the y direction (which is of less interest in a tokamak), the situation is reversed.

V. POLOIDAL SHEAR FLOW EFFECTS

So far, we have focused on the impact of anisotropic vortical structures (streamers) on the radial (and poloidal) diffusivities of trace ions. Such considerations are known to apply, e.g., to trapped electron mode (TEM) turbulence.[14] However, in the case of ion temperature gradient (ITG) driven turbulence, the system usually spins up poloidal shear flows to fairly high amplitudes (see Ref. [23] and references therein). Thus it is interesting to investigate the effect of such zonal flows on trace ion transport.

As a model potential, we choose

$$\tilde{\phi}(x,y,t) = \phi(x,y,t) + A_{\rm zf}\sin(k_{\rm zf}x)\,. \tag{13}$$

Here, ϕ represents the isotropic potential considered already in Sec. III and generated according to Eq. (1) with $N = 10^3$. The corresponding Eulerian autocorrelation function is then easily shown to be

$$\tilde{E}(x,y,t) = E(x,y,t) + \frac{A_{\rm zf}^2}{2}\cos(k_{\rm zf}x)\,, \tag{14}$$

where E is the autocorrelation of ϕ. Unfortunately, it is not possible to easily extend the scaling approach introduced in Sec. III to cases with strong zonal flows. This is because the last term in Eq. (14) completely changes the shape of the autocorrelation, leading to a minimum with large negative values on the x axis and to a plateau on the y axis. Qualitatively, one can expect that the presence of poloidal shear flows will bring about a reduction (an increase) of the diffusivity in the x (y) direction since negative values of $\tilde{E}$ make it less probable for an equipotential line to cross that region, whereas a plateau indicates a larger crossing probability. Quantitative statements have to rely on numerical simulations. But before we turn to those, we would like to insert a brief discussion about the influence of finite gyroradius effects on the transport properties. In this context, one finds the effective autocorrelation function

$$\tilde{E}^{\rm eff}(x,y,t) = E^{\rm eff}(x,y,t) + \frac{A_{\rm zf}^2}{2}\cos(k_{\rm zf}x)J_0^2(k_{\rm zf}\rho)\,, \tag{15}$$

i.e., the generic structure of the autocorrelation function is preserved. As we know from Sec. III, finite gyroradius effects enhance the correlation length inferred from $\tilde{E}^{\rm eff}$ – but they have no influence on the wavelength of the zonal flow term in Eq. (15), of course. Considering both terms together, one can thus expect that the gyroaveraging process will lead to an increase of the (effective) correlation length, but this increase will be more moderate than for a potential without zonal components. Moreover, since for realistic parameters, $k_{\rm zf}$ is usually smaller than the average value of $|\mathbf{k}_i|$, the influence of the zonal flow term will increase with increasing gyroradius as long as $k_{\rm zf}\rho \lesssim 1$. So what we expect for the ρ dependence of the transport is a reduction of the plateau regime observed in Figs. 1 and 2.

Let us now turn to the numerical simulation results. Here, the isotropic potential is created the same way as in Sec. III, and the zonal flow is characterized by $k_{\rm zf} = 0.76$

and $A_{\rm zf}^2/2 = 0.6\,E(0)$. The latter values are inspired by data from gyrokinetic turbulence simulations with the GENE code.[13, 14] The resulting diffusion coefficient for the x direction is shown in Fig. 9 for different Kubo numbers and gyroradii. We have chosen the isotropic Kubo number K_I as a parameter, since the Kubo number including the zonal flow term is not unique in the x and y direction any more. However, as follows from Eqs. (6) and (7) (note $V_x = (-\partial^2 \tilde{E}(\mathbf{x},t)/\partial y^2|_{\mathbf{x}=t=0})^{1/2} = (-\partial^2 E(\mathbf{x},t)/\partial y^2|_{\mathbf{x}=t=0})^{1/2}$ and the fact that λ_x is only marginally affected by the zonal flow term), $K_x \approx K_I$. The Kubo number is then again varied by changing τ_c in the isotropic component of the potential.

Compared to Fig. 1, we notice two main differences. First, for $K > 1$, the reduction of D_x with K is stronger ($\gamma \approx 0.6$). This is due to the strong negative values of $\tilde{E}^{\rm eff}$, indicating – in the Eulerian picture – that there is a 'transport barrier.' Second, we see that for $K > 1$, a slight reduction of D_x with ρ remains even for $\rho < 1$. This finding is in qualitative agreement with the prediction we made above, studying the effective correlation lengths. The curves for $\rho = 3$ and $\rho = 10$ play a special role. Here, the gyroaveraging filters out the zonal flow term due to $J_0(k_{\rm zf}\rho) \approx 0$, and the $D_x(K)$ curve follows the curve for the pure isotropic case shown in Fig. 1. However, this is a direct consequence of our simple choice for the model potential which only features a single zonal mode. In practice, there will always be a superposition of many zonal modes, weakening this effect. In the y direction, on the other hand, the situation is completely different. Here, the particle diffusivity is *increased* by the zonal flow term, and $D(t \to \infty)$ increases further for $\rho \lesssim 1$ when ρ is increased.

The results obtained in the present section may be expected to be prototypical for a large class of systems which can be described as a superposition of background turbulence and zonal flows. They show that the radial particle transport tends to be inhibited by strong zonal flows – as expected – and that the finite gyroradius effects still differ in the low and high Kubo number regimes.

VI. POLOIDAL DRIFT EFFECTS

While it is not hard to understand (given the huge amount of literature on this topic) that *sheared* poloidal flows can lead to a strong suppression of the radial fluxes of trace species, it is probably easy to overlook that *homogeneous* poloidal drifts may have the same effect. This will be the topic of the present section.

Generally, all microinstabilities in toroidal magnetoplasmas exhibit drifts in the poloidal direction. While ion temperature gradient (ITG) modes tend to drift in the ion diamagnetic direction, electron temperature gradient (ETG) modes and trapped electron modes usually drift in the electron diamagnetic direction. It should be kept in mind, however, that it is also possible for these modes to have only very small drift velocities or even change their drift direction. This is often the case when the gradients which are not responsible for the main drive of the respective mode (e.g., the electron temperature gradient in the case of ITG modes) are increased. As we have found in many GENE simulations, these linear drifts tend to carry over into the nonlinear, fully turbulent regime, at least as far as the long-wavelength modes are concerned, i.e., the ones typically responsible for most of the turbulent transport.

In the context of our present stochastic model, we want to define as a 'drifting potential' ϕ_{dr} a (fluctuating or static) potential whose structures move in the poloidal (y) direction with a constant drift velocity v_{dr}. Denoting again the isotropic potential from Sec. III by $\phi(x, y, t)$, we thus have

$$\phi_{\mathrm{dr}}(x, y, t) \equiv \phi(x, y - v_{\mathrm{dr}}t, t)\,. \tag{16}$$

As we will see in the next section, the model described by Eq. (16) is fairly realistic and represents an important and new class of transport effects. Simulations show that the introduction of a drift velocity v_{dr} of the order of V in the y-direction reduces transport in the x direction by up to one order of magnitude, whereas it strongly enhances the transport in the y direction.

A. Zero gyroradius limit

In order to understand the effect of such a homogeneous drift, it is useful to perform a Galilei transformation to a reference frame moving in the y direction with velocity v_{dr}. Quantities referring to this co-moving coordinate system will be denoted with a prime. Using Faraday's law of induction (in the limit of non-relativistic velocities) this transformation leads to an additional component of the electrostatic field,

$$\mathbf{E}' = \mathbf{E} + \mathbf{v}_{\mathrm{dr}} \times \mathbf{e}_{\mathbf{z}}. \tag{17}$$

Note that due to our normalization $\mathbf{B}$ is replaced by $\mathbf{e}_z$. Rewriting this equation in terms of the electrostatic potential ($\mathbf{E} = -\nabla\phi$), we thus find

$$\phi'_{\rm dr}(x, y, t) = \phi_{\rm dr}(x, y + v_{\rm dr}t, t) - v_{\rm dr}x = \phi(x, y, t) - v_{\rm dr}x\,. \tag{18}$$

For the particle motion we then find the (trivial) relation $\mathbf{v}'_E = \mathbf{v}_E - v_{\rm dr}\mathbf{e}_y$. So in the co-moving frame, which is more easy to access, the law of induction produces an additional electric field, which is responsible for the different behavior compared to a non-drifting potential. An example for such a drift frame potential is shown in Fig. 10. It is clear that the second term on the right-hand side of Eq. (18) gives the potential a completely new structure. Since it represents an infinite ramp, it prevents the formation of long-ranged equipotential lines in the x direction, whereas open equipotential lines running in the y direction are favoured. If we denote the maximum absolute value of the potential ϕ by $\phi_{\rm max}$, we can estimate from Eq. (18) the maximum length of an equipotential line in the x direction to be $x_{\rm max} \approx 2\phi_{\rm max}/v_{\rm dr} \approx 2\,V\lambda_c/v_{\rm dr}$ (here, λ_c is the correlation length of ϕ, and V is the average $E\times B$ drift velocity). Since for a non-fluctuating (but drifting) potential $\phi_{\rm dr}(x, y, t) = \phi(x, y-v_{\rm dr}t)$, the length of the trajectory is limited in the x direction, we expect the diffusion coefficient to show a sharp drop to zero. The 'drop time' can be estimated by the time a particle needs to cross the maximum trajectory length, $\tau_{\rm drop} \approx x_{\rm max}/V = 2\lambda_c/v_{\rm dr}$. Simulation results show a good correspondence with this estimate (see Fig. 11). Comparing a fluctuating potential (finite τ_c or K) with a non-fluctuating potential ($\tau_c, K \to \infty$), the typical behavior is that the $D(t)$ curves are almost identical for $t \lesssim \tau_c$, whereas for $t \gtrsim \tau_c$, the curve for the fluctuating potential departs from the $K = \infty$ curve and saturates.[9, 18] Thus we expect that for $\tau_c \gtrsim \tau_{\rm drop}$ or $v_{\rm dr} \gtrsim 2\lambda_c/\tau_c$, the diffusion will be strongly reduced also at finite K, since in that case, the barrier life time exceeds the time a particle needs to travel the distance $x_{\rm max}$. On the other hand, as long as $v_{\rm dr} \ll \lambda_c/\tau_c$, the influence of the homogeneous drift on D_x is relatively small.

Noting that in the drifting frame, the particles follow the isolines of $\phi'_{\rm dr}$, Fig. 10 tells us that there are two different classes of particles: trapped ones which in the lab frame move in the y direction with the drift velocity $v_{\rm dr}$ – and passing ones which (even in the lab frame) move against the drift into the negative y direction. The former dominate for small drift velocities, whereas the latter prevail for large drift velocities when the second term in Eq. (18) dominates. Considering the drift frame potential, it is also clear that

trapped particles will be found primarily near the extremas of ϕ, whereas particles on open trajectories will be found near $\phi \approx 0$. Such a behavior has already been reported in Ref. [8].

Since in the lab frame, we have $\langle \partial_x \phi_{\rm dr} \rangle = 0$ due to symmetry arguments, the quantity $\langle [y(t) - y(0)] \rangle$ always stays zero. This means that the weighted distance of the trapped particles moving into the positive y direction and of the untrapped particles moving into the negative y direction keeps constant. Given that the (average) velocity of the trapped particles is $V_y^{\rm trapped} = v_{\rm dr}$ in the lab frame, the average velocity of the untrapped particles has to be $-V_y^{\rm untrapped} = v_{\rm dr} N^{\rm trapped}/N^{\rm untrapped}$. As $N^{\rm trapped}$ gets smaller when $v_{\rm dr}$ is increased, it is possible for the average velocity of the untrapped particles to stay constant over a certain range of drift velocities. In Fig. 12, we display the probability distribution function (PDF) for the particle position in the y direction at a fixed time for a static potential and a series of different drift velocities $v_{\rm dr}$. Sharp peaks of trapped particles can be clearly observed which move to the right with $v_{\rm dr}$, whereas the untrapped particles move to the left (on average). The average velocity of the untrapped particles is observed to stay approximately constant for $v_{\rm dr} \lesssim V$ as pointed out above. Further, it can be estimated that the maximum of $v_{\rm dr} N^{\rm trapped}$ is reached for $V \approx v_{\rm dr}$ which can be interpreted as a resonance condition.

Since we have chosen a static potential, particles stay trapped or untrapped forever. If we introduce a time dependence of the fluctuations, the structures are not constant in time, so that trapped particles can become untrapped and vice versa. This, of course, leads to a dispersion of the structures in the PDF with time increasing. For very large times, the PDF turns into a Gaussian.

B. Finite gyroradius effects

As before, we would like to also study the influence of finite gyroradius effects. To this aim, one has to consider effective gyroaveraged potentials instead of the ones used above. Since the second term on the right-hand side of Eq. (18) is not affected by gyroaveraging, we find

$$\phi'^{,\rm eff}_{\rm dr}(x,y,t) = \phi^{\rm eff}(x,y,t) - v_{\rm dr} x \,. \tag{19}$$

It thus follows that the effective correlation lengths and drift velocities are simply the ones obtained in the isotropic case (see Sec. III). Consequently, λ_c increases and V decreases with increasing gyroradius ρ. At the same time, since the gyroaveraging reduces the absolute

values of ϕ, the second term in Eq. (19) becomes more dominant – which means that the number of trapped particles is reduced with growing ρ.

Fig. 11 shows the running diffusion coefficient in the x direction for $v_{\mathrm{dr}} = 0.0013$ (for comparison, $V = 0.0052$) for a number of different gyroradii normalized to the correlation length of the potential. The solid lines are obtained from a static (but still drifting) potential. Like discussed above, the diffusion is bound to drop to zero for large times. As can be inferred from the figure, the drop time is well approximated by the expression derived above, $\tau_{\mathrm{drop}} \approx 2\lambda_c/v_{\mathrm{dr}}$. In particular, since λ_c grows with increasing ρ, τ_{drop} grows, too. These considerations for a static potential enable us to also interprete the behavior of $D(t)$ for a fluctuating potential. The dashed lines in Fig. 11 show such curves for $K = 18$ and $\tau_c \approx 3000$. As we have already mentioned, the $D(t)$ curves for finite K follow the curves for the static potential up to $t \sim \tau_c$, and then they saturate. In our example, we have $\tau_c \approx \tau_{\mathrm{drop}}$ which is in line with data obtained from GENE simulations of (pure) trapped electron mode turbulence (see Ref. [14] and the results presented in the next section). Since the curves for static potentials in Fig. 11 lie close to each other for $t \approx \tau_c$, we can understand why the same is true for time fluctuating potentials. However, as the curves for small gyroradii tend to saturate earlier than the ones for larger gyroradii, this argument is more a qualitative one. We remark that again we have found a regime where the diffusion keeps constant for $\rho \lesssim 1$, and again this effect is due to the increase of the effective correlation length. However, the mechanism leading to this result is different from the one discussed in Sec. III.

The effect that the different curves do not saturate at exactly the same time although their correlation time is the same is a consequence of a more fundamental effect. In simulations varying the correlation time as well as the Kubo number we found that for $K < 1$, the saturation time coincides quite well with the correlation time, whereas for $K > 1$, the saturation time is reduced compared to τ_c. Thus, the stronger the trapping (i.e., the more circulations around a certain eddy a particle can perform), the more sensitive its motion with respect to small perturbations. In Ref. [20], the lifetime τ_h of the contour $\phi = h \ll 1$ (with the maximum of the potential normalized to unity) is estimated by the expression $\tau_h \approx h\tau_c$. Since we know that for large Kubo numbers, the transport is dominated by large-scale trajectories with $h \sim 0$, this confirms our observation. Consequently, an increase of the gyroradius leads to a reduction of the effective Kubo number (see Sec. VII A), and the saturation time increases – although the correlation time stays the same. If, like in our case,

$\tau_c \approx \tau_{\rm drop}$, small changes in the saturation time can cause large changes in the saturation value of D, since the $D(t)$ curve for the static potential changes rapidly around that time. In Fig. 11, the increase of D for the static potential is balanced by the slight increase of the saturation time, leading to approximately the same saturation value for different, but small gyroradii.

Fig. 13 displays the running diffusion coefficient in the y direction for the same potential as in Fig. 11. In the static case (solid lines), we see that the transport is ballistic for large times. Here, the trapped particles move with the drift velocity, whereas – as we have shown above – the untrapped particles move with a constant average velocity into the opposite direction. We have also seen that an increase of the gyroradius leads to a reduction of both the number of trapped particles and the average velocity of the untrapped particles ($-V_y^{\rm untrapped} = v_{\rm dr} N^{\rm trapped}/N^{\rm untrapped}$). Since the average velocity $\overline{V}_y \equiv (N^{\rm trapped}|V_y^{\rm trapped}| + N^{\rm untrapped}|V_y^{\rm untrapped}|)/N = (2N^{\rm trapped}/N)\, v_{\rm dr}$ does not depend on the effective correlation length but only on the number of trapped partices (and, of course, on the drift velocity), one may expect that D_y drops already for small gyroradii. Fig. 13 supports this claim.

VII. TRACE IONS IN REALISTIC TURBULENT FIELDS

Until now, we have studied the transport of passive tracers in electrostatic potentials which were created by superposing a large number of plane waves. Applying this method, we were able to model and study a wide number of different effects including anisotropies, zonal flows, poloidal drifts as well as their dependence on the Kubo number of the potential and the gyroradius of the particles. With these results in our hands, we are now in a good position to examine passive tracer transport in realistic turbulent potentials obtained from nonlinear gyrokinetic simulations. Here, some or all of the above effects may be present at the same time and interact with each other.

As an example, we will use simulation data for trapped electron mode (TEM) turbulence in tokamaks obtained with the nonlinear gyrokinetic code GENE [13, 14]. As plasma parameters we use the nominal values listed in Sec. II.B of Ref. [14]. The electrostatic potential in a perpendicular plane on the low-field side is written out frequently and then subjected to post-processing. In this context, it is necessary to make a few remarks about the box and grid size as well as the employed discretization methods. First, GENE uses doubly

periodic boundary conditions. So to exclude finite box size effects, we choose a simulation domain whose extensions in the x and y directions are much (about 25 times) larger than the respective correlation lengths. This helps to avoid spurious potential correlations and particle trajectories. Second, the choice of the discretization methods was found to be of great importance. Given (only) the electrostatic potential (only) on a two-dimensional x-y grid, it is necessary both to calculate the $E\times B$ drift velocities (i.e. the spatial derivatives), and to interpolate between the grid points (for an overview on commonly used interpolation schemes, see Ref. [24]). We found that the only method ensuring closed trajectories for static potentials is to both differentiate and interpolate in Fourier space. When using other, numerically less expensive interpolation schemes (e.g., bicubic interplation), the trajectories are not closed any more. Although the differences between Fourier and bicubic interpolation tend to be small as long as one is merely interested in *statistical* quantities (like diffusion coefficients) for *time-dependent* potentials, we still prefer to work with the Fourier method – it is most accurate (and works for any Kubo number) while sufficiently effective for our purposes.

We note that from now on, perpendicular length scales are normalized with respect to $\rho_s = c_s/\Omega_i$ where $c_s = (T_e/m_i)^{1/2}$ is the ion acoustic velocity and Ω_i the ion gyrofrequency, whereas time scales are normalized with respect to $L_\perp/c_s$ where $L_\perp$ is a scale length of the background profiles (see, e.g., Ref. [14]). The measured correlation lengths of the potential which will be used for our test particle studies are $\lambda_x = 6.1$ and $\lambda_y = 4.2$. Fig. 14 displays the contours of the autocorrelation function of this potential plotted versus the coordinate y and time t. It can clearly be observed that while decaying to zero for large times and distances, the whole potential moves in the positive y direction with a velocity of about $v_{\rm dr} = 0.95$. The components of the average $E\times B$ drift velocity are found to be $V_x = 3.3$ and $V_y = 2.3$. Since $\tau_c \approx 15$ in the co-moving frame, we have $v_{\rm dr} \sim 2\lambda_c/\tau_c$ ($\tau_c \sim \tau_{\rm drop}$), and poloidal drift effects are expected to be significant. In a first step, however, we will consider a modified potential for which the drift has been removed. Drift effects will then be included in a second step.

A. First step: Neglecting poloidal drift effects

As was discussed above, the existence and magnitude of a poloidal drift depends on the simulation parameters. Linear gyrokinetic simulations show that if R/L_{T_e} and R/L_{T_i} become comparable, the phase and group velocities of ITG modes or TEMs tend to be rather small. We model such a situation by removing the drift from the original potential, i.e., we work with a new potential $\phi'(x, y, t) \equiv \phi(x, y + v_{\mathrm{dr}}t, t)$ where $v_{\mathrm{dr}} = 0.95$. Using ϕ', we perform test particle simulations for a set of different gyroradii and discuss the results in the light of the experience we made in Secs. IV and V.

Fig. 15 shows the wavenumber spectrum of the TEM potential. We observe a maximum around $|k_y| \sim 0.2$ and $k_x \sim 0$. Since those modes play a prominent role, the autocorrelation function takes on negative values on the y axis in real space around $|y| \sim \pi/0.2 \sim 16$. Obviously, we have $\lambda_x > \lambda_y$, which means that the turbulence exhibits streamers (radially elongated eddies). However, one also observes that that there is significant activity for finite values of k_x – which is important for the understanding of finite gyroradius effects. As we have already discussed in detail, the effective autocorrelation function is obtained by multiplying the spectrum with $J_0^2(k\rho)$. In Fig. 15, the $J_0^2 = 1/e$ line and the line of the first zero crossing are plotted for $\rho = 6$. Transforming the gyroaveraged spectra back to real space, one observes an increase of both λ_x and λ_y with increasing gyroradius, reaching their maximum values for $\rho = 6$. However, the increase is much larger in the x direction – in contrast to the findings in Sec. IV where a Gaussian potential was considered. Here, the dominating finite k_y mode is not affected much by the gyroaveraging process, thus leaving λ_y more or less unchanged. This effect is somewhat similar to the one found in the zonal flow model studied in Sec. V – only that the roles of the x and y directions are reversed. The increase of λ_x is due to the long tails of the spectrum in the k_x direction which are removed under the influence of the Bessel function.

Fig. 16 shows the running diffusion coefficient in both directions for a set of different gyroradii. One first notices that the diffusion is smaller in the y direction than in the x direction. This effect can be explained by remembering that the autocorrelation spectrum is characterized by $\lambda_x > \lambda_y$ and the existence of a dominating finite k_y mode. From Secs. IV and V, we already know that both effects lead to a relative decrease of the transport in the y direction. Furthermore, we observe that D_x is roughly constant for $\rho \lesssim 3$ (remember

$\lambda_x \approx 6$) and then falls off as ρ is increased further. D_y, on the other hand, is reduced already for small gyroradii. However, this reduction is more moderate for larger ρ than that in the x direction. The ρ dependence of D_x can be interpreted via Fig. 17 where the saturation values of D_x (taken from Fig. 16) are plotted together with the estimates obtained from the formula $D_\rho/D_0 = (\lambda^{\text{eff}}/\lambda_0)^{2-\gamma}(V^{\text{eff}}/V_0)^\gamma(\tau^{\text{eff}}/\tau_0)^{\gamma-1}$ (see Secs. III and IV, noting that now an effective correlation time has to be taken into account, too, since the frequencies are no longer independent of the wavenumbers). The effective values have been extracted from the gyroaveraged autocorrelation function as before. In the small and large Kubo number limit, we have used $\gamma = 2$ and $\gamma = 0.7$, respectively. As we can infer from Fig. 17, the simulation results follow the high Kubo number expectations quite well for small gyroradii, whereas they tend to approach the low Kubo number limit for larger values of ρ. (We note in passing that since $K = 8.6$ for the present case, we cannot expect that the large Kubo number limit is fully established.) This behavior can be understood by introducing effective (i.e., ρ dependent) Kubo numbers, $K^{\text{eff}} = \tau^{\text{eff}} V^{\text{eff}}/\lambda^{\text{eff}}$, and taking into account that γ can vary between 2 (linear regime) and about 0.7 (nonlinear regime). K^{eff} will decrease rapidly if ρ is increased since V^{eff} decreases but λ^{eff} grows. Once K^{eff} approaches unity, we expect the effective value of γ to increase. This fact qualitatively explains the behavior of the simulation results shown in Fig. 17. In search of a more quantitative approach, we determined a function $\gamma(K^{\text{eff}}(\rho))$. To this aim, we modified the original TEM data by rescaling the length of the time intervals between the successive steps written out by GENE. This manipulation enabled us to vary the correlation time and therefore the Kubo number of the TEM potential. We then compared the values of $K^{\text{eff}}(\rho)$ with the expression $D(K) = a(K)\, K^{\gamma(K)-1}$ to obtain $\gamma(\rho)$ and $a(\rho)$. Thus, one gets

$$D_\rho/D_0 = \frac{a_\rho \lambda_\rho^{2-\gamma_\rho} V_\rho^{\gamma_\rho} \tau_\rho^{\gamma_\rho - 1}}{a_0 \lambda_0^{2-\gamma_0} V_0^{\gamma_0} \tau_0^{\gamma_0 - 1}}\,. \tag{20}$$

The corresponding values are shown as a dashed line in Fig. 17. Obviously, they are in good agreement with the simulation results, demonstrating that the form of D_ρ/D_0 is well captured by our effective autocorrelation function approach for a large class of potentials.

B. Second step: Including poloidal drift effects

Having discussed the behavior of trace ions in a realistic turbulence potential for which poloidal drift effects have been removed, we would now like to include the latter. With $v_{\rm dr} = 0.95$, we find $\tau_{\rm drop} = 12.8$ which is fairly close to the correlation time $\tau_c = 15$ (a similar case has been considered in Sec. VI). In Fig. 18, the running diffusion coefficients D_x and D_y are plotted for a set of different gyroradii. The results are reminiscent of those in self-generated drifting potentials shown in Figs. 11 and 13. First, we observe that D_y is enhanced and D_x is reduced compared to the case with $v_{\rm dr} = 0$ shown in Fig. 16. The physical origin of this behavior has already been identified in Sec. VI. Again we have the situation that $\tau_{\rm drop} \approx \tau_c$ which means that the decorrelation process – the transition into the diffusion regime – occurs in the time segment where the variation of D_x is large. Therefore the saturated value of D_x depends quite sensitively on the saturation time.

In Sec. VI, we have already made the observation that the saturation time gets larger compared to the correlation time as the (effective) Kubo number gets smaller, i.e., as the gyroradius increases. In Fig. 18, this effect seems to be stronger than in Fig. 11; although for $t \sim \tau_{\rm drop}$, the curves for different ρ lie close to each other, the saturation values decrease rapidly even for small ρ. So in contrast to the case described in Sec. VI, we have here the situation that poloidal drift effects lead to a stronger reduction of the diffusion with increasing gyroradius, illustrating the subtle interactions between finite gyroradius and poloidal drift effects. In this context, we would like to point out that for realistic turbulence potentials (like the one considered here) the gyroaveraging also affects the correlation time since the wavenumbers and frequencies of the individual modes are correlated. For example, for $\rho = 3$, the correlation time is increased by a factor of about 1.1, which of course provides a contribution to the increase of the saturation time. – In the y direction, one observes a strong reduction of D_y with incrasing ρ compared to Fig. 13. This effect has already been described in Sec. VI, where we found that it is due to the reduction of the number of trapped particles in the effective potential.

VIII. SUMMARY AND CONCLUSIONS

The main goal of the present work was to investigate the behavior of trace ions in realistic turbulent fields, focussing on the various physical effects determining their particle diffusivities. For simplicity, we have restricted to electrostatic fluctuations and two dimensions as far as the particle trajectories are concerned. Nevertheless, we have used electrostatic potentials taken from three (space) dimensional gyrokinetic simulations with the GENE code. As an example, trapped electron mode turbulence was chosen. In order to be able to study several individual effects in isolation, we also considered potentials which were generated by superposing a large number of random waves. These supplementary studies helped to gain a basic understanding of trace ion transport which is crucial for interpreting the gyrokinetic data.

Using self-generated potentials, we found that for isotropic turbulence, the diffusivity stays constant for gyroradii up to the correlation length of the potential for large Kubo numbers (strong turbulence), whereas it falls off quite rapidly for small Kubo numbers (weak turbulence). Moreover, we found that fluctuation anisotropies like streamers (radially elongated vortices) and zonal flows (poloidal shear flows) may strongly influence the resulting transport levels as well as the gyroradius dependence. Here, the transport may decrease faster or even grow as the gyroradius is increased. Finally, we have shown that poloidal drift effects can have a strong impact on the particle diffusion, enhancing it in the direction of the drift and reducing it in the other (radial) direction. Although the underlying mechanisms are different than for non-drifting potentials, regimes can still be found in which the transport stays constant for gyroradii up to a correlation length.

In many cases, there exist subtle interactions between various effects (e.g., finite gyroradius and finite poloidal drift), leading to fairly complex behavior. Nevertheless, we were able to demonstrate that the diffusivities obtained from tracking particle trajectories in realistic turbulence potentials are usually well described and understood in terms of simple scaling laws employing (effective) correlation lengths, correlations times, and Kubo numbers. This information can be extracted from the autocorrelation function of the (gyroaveraged) potential. Thus, one obtains a fairly coherent picture of (perpendicular) trace ion transport in turbulent plasmas.

Our present work has implications for various situations in which one is interested in the

turbulent transport of trace ions. First, finite gyroradius effects do not necessarily lead to a reduction of the particle diffusivity – at least as long as the gyroradius does not exceed the correlation length(s). Similar arguments are expected to apply to drift orbit shift effects on passing particles in three dimensions. Second, the radial diffusion exhibits a strong dependence on the magnitude of the fluctuations' poloidal drift velocity. This effect may – in practice – often be more important than the presence of zonal flows.

Acknowledgments

We thank F. Merz, M. Püschel, and T. Görler for providing simulation data obtained with the gyrokinetic turbulence code GENE. We are also grateful to S. Günter for stimulating discussions.

[1] R. Balescu, *Aspects of Anomalous Transport in Plasmas* (IoP Publishing, Bristol, 2005).

[2] V. Naulin, A. H. Nielsen, and J. J. Rasmussen, Phys. Plasmas **6**, 4575 (1999).

[3] R. Basu, T. Jessen, V. Naulin, and J. J. Rasmussen, Phys. Plasmas **10**, 2696 (2003).

[4] B. Scott, Phys. Plasmas **12**, 082305 (2005).

[5] C. Estrada-Mila, J. Candy, and R. E. Waltz, Phys. Plasmas **13**, 112303 (2006).

[6] G. Manfredi and R. O. Dendy, Phys. Rev. Lett. **76**, 4360 (1996).

[7] G. Manfredi and R. O. Dendy, Phys. Plasmas **4**, 628 (1997).

[8] S. V. Annibaldi, G. Manfredi, and R. O. Dendy, Phys. Plasmas **9**, 791 (2002).

[9] T. Hauff and F. Jenko, Phys. Plasmas **13**, 102309 (2006).

[10] Z. Lin, L. Chen, and F. Zonca, Phys. Plasmas **12**, 056125 (2005).

[11] D. del-Castillo-Negrete, Phys. Plasmas **7**, 1702 (2000).

[12] E. A. Frieman and L. Chen, Phys. Fluids **25**, 502 (1982).

[13] F. Jenko, W. Dorland, M. Kotschenreuther, and B. N. Rogers, Phys. Plasmas **7**, 1904 (2000).

[14] T. Dannert and F. Jenko, Phys. Plasmas **12**, 072309 (2005).

[15] J. H. Reuss, J. D. and Misguich, Phys. Rev. E **54**, 1857 (1996).

[16] F. J. Vesely, *Computational Physics*, Ch. I 4 (Plenum Press, New York, 1994).

[17] R. Kubo, J. Math. Phys. **4**, 174 (1963).

[18] M. Vlad, F. Spineanu, J. H. Misguich, J. D. Reuss, R. Balescu, K. Itoh, and S. I. Itoh, Plasma Phys. Control. Fusion **46**, 1051 (2004).

[19] J. D. Reuss, M. Vlad, and J. H. Misguich, Phys. Lett. A **241**, 94 (1998).

[20] A. V. Gruzinov, M. B. Isichenko, and Y. L. Kalda, Sov. Phys. JETP **70**, 263 (1990).

[21] M. B. Isichenko, Rev. Mod. Phys. **64**, 961 (1992).

[22] B. B. Kadomtsev, *Plasma Turbulence*, Ch. IV 4 (Academic, London, 1965).

[23] P.H. Diamond, S.-I. Itoh, K. Itoh, T.S. Hahm, Plasma Phys. Control. Fusion **47**, R35 (2005).

[24] P. K. Yeung and S. B. Pope, J. Comput. Phys. **79**, 373 (1988).

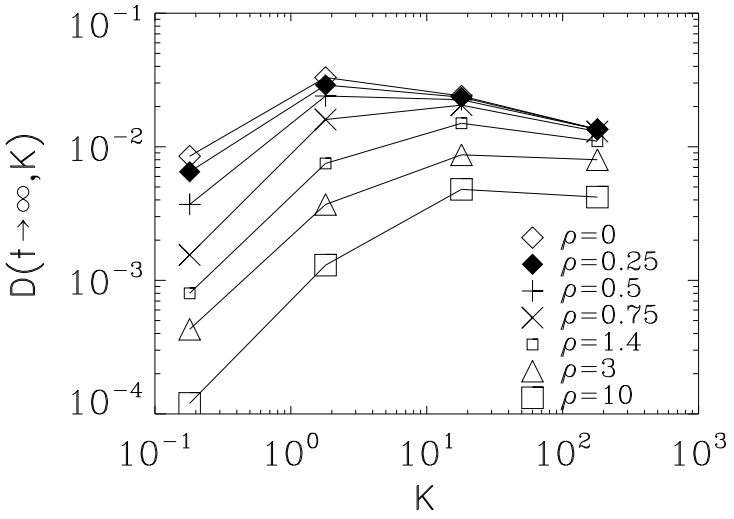

FIG. 1: Long-time limit of the diffusivity D as a function of the Kubo number K for different gyroradii ρ (normalized to the correlation length of the potential) in an isotropic stochastic potential.[9]

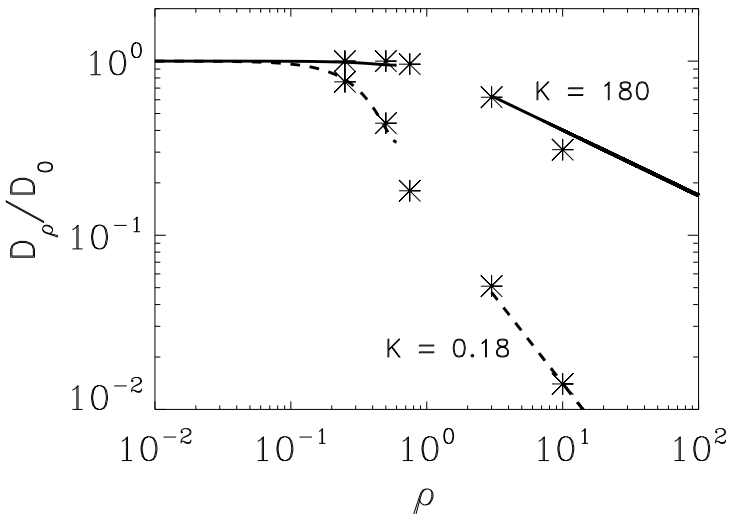

FIG. 2: Comparison between the numerically determined diffusion coefficients of Fig. 1 and the analytical formulas of Eqs. (10) and (11). Here, D_0 and D_ρ denote, respectively, the diffusivity for vanishing and finite gyroradius.[9]

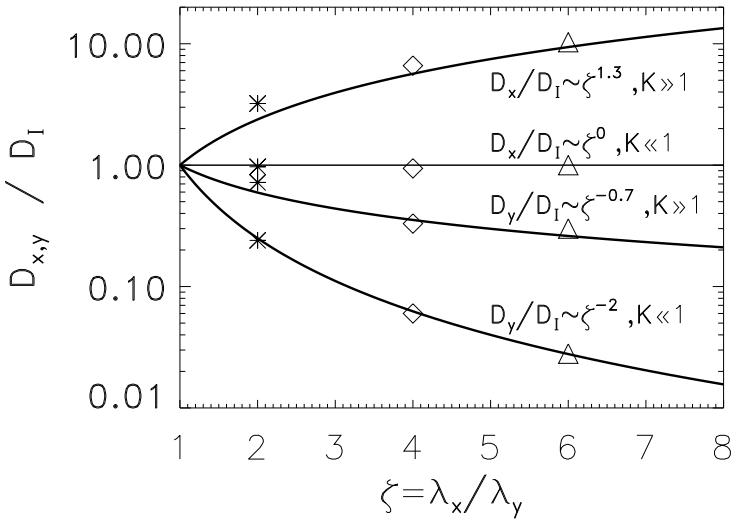

FIG. 3: Ratio of the diffusion coefficients in anisotropic ($D_{x,y}$) and isotropic (D_I) stochastic turbulence versus the 'anisotropy factor' $\zeta = \lambda_x/\lambda_y$. Solid curves: analytical approach in the low/high Kubo number limit; single points: simulation results for $K_I = 0.07$ and $K_I = 70$.

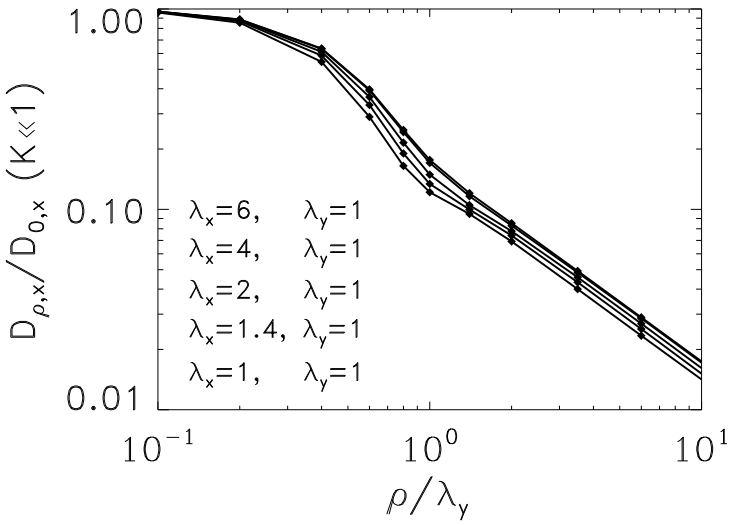

FIG. 4: Relative diffusion $D_{\rho,x}/D_{0,x} = (V_{\rho,x}/V_{0,x})^2$ (semi-analytical approach) for $K \ll 1$ and different anisotropies $\zeta = \lambda_x/\lambda_y$. The subscripts ρ and 0 denote, respectively, cases with finite and vanishing gyroradius. The parameters in the legend correspond to the order of the curves.

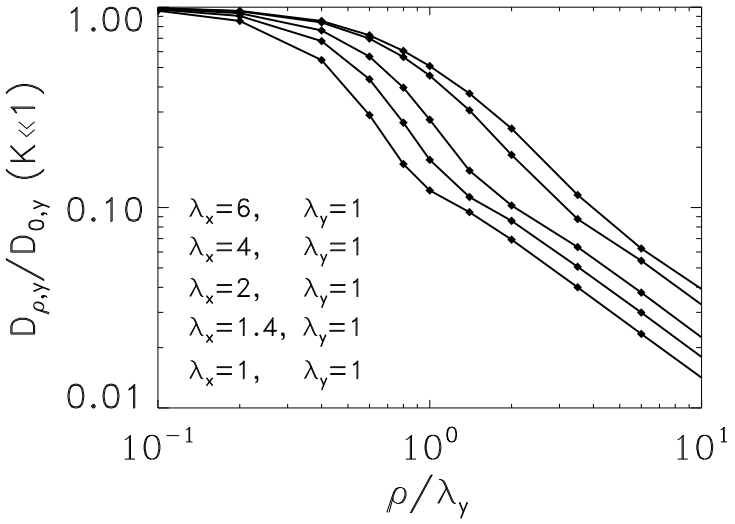

FIG. 5: Same as Fig. 4, but for the y direction.

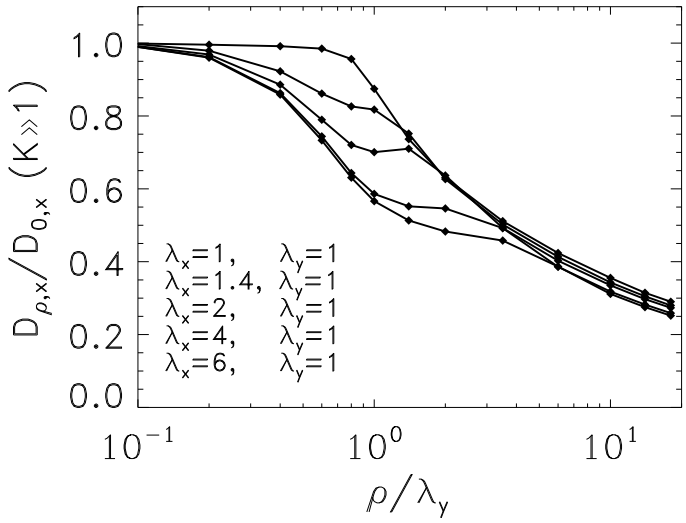

FIG. 6: Relative diffusion $D_{\rho,x}/D_{0,x} = (V_{\rho,x}/V_{0,x})^{\gamma}(\lambda_{\rho,x}/\lambda_{0,x})^{2-\gamma}$, $\gamma = 0.82$ (semi-analytical approach) for $K \gg 1$ and different anisotropies $\zeta = \lambda_x/\lambda_y$. The subscripts ρ and 0 denote, respectively, cases with finite and vanishing gyroradius. The parameters in the legend correspond to the order of the curves.

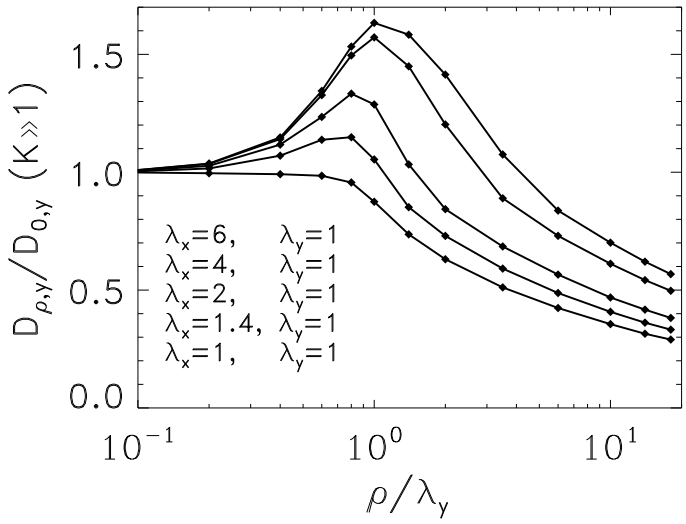

FIG. 7: Same as Fig. 6, but for the y direction. Here, $\gamma = 0.72$.

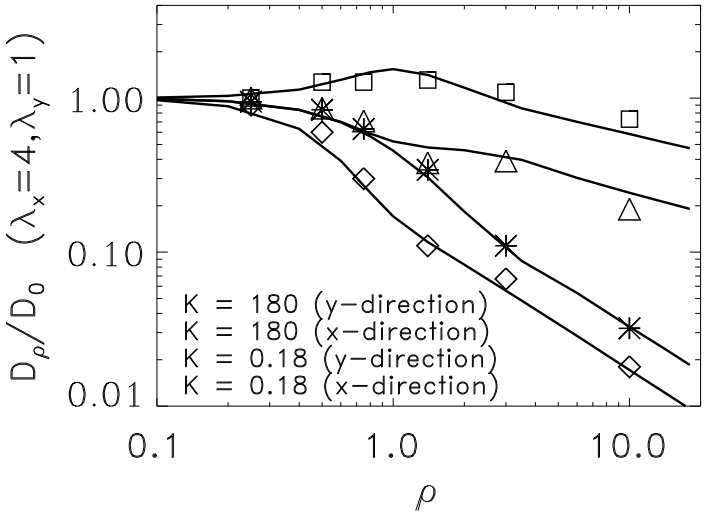

FIG. 8: Comparison between the simulation results (symbols) for an anisotropic potential with $\zeta = \lambda_x/\lambda_y = 4$ and the semi-analytical approach (solid lines; data taken from Figs. 4 through 7) for $K \ll 1$ and $K \gg 1$. The parameters in the legend correspond to the order of the curves.

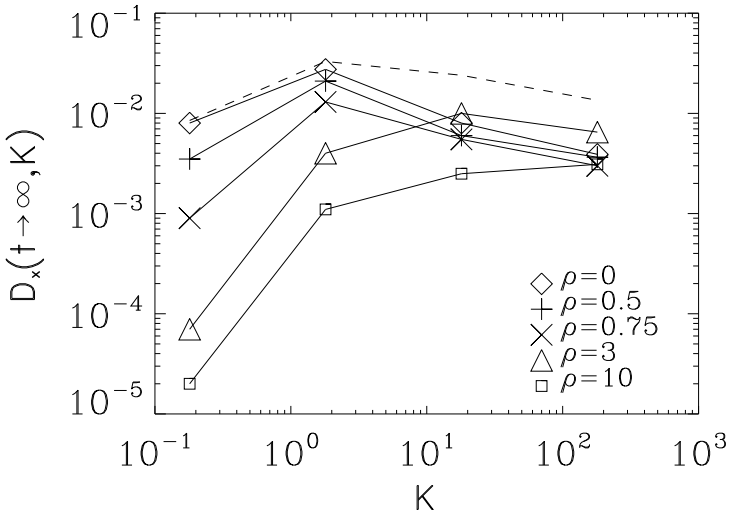

FIG. 9: Long-time limit of the diffusivity D_x as a function of the Kubo number K for different gyroradii ρ (normalized to the correlation length of the potential) in a potential with a superposed zonal flow [see Eq. (13)]. The dashed line represents the case for $\rho = 0$ without zonal flow (data taken from Fig. 1).

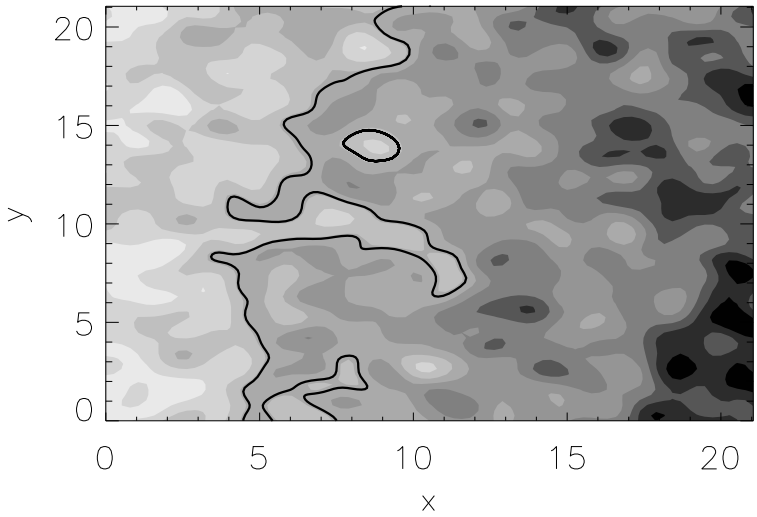

FIG. 10: Contour plot of the effective (static) potential in the drifting frame, $\phi'_{\rm dr}$, for a poloidal drift velocity of $v_{\rm dr} = 0.0013$ ($V = 0.0052$). Representative open and closed isolines (particle trajectories) are shown as solid lines.

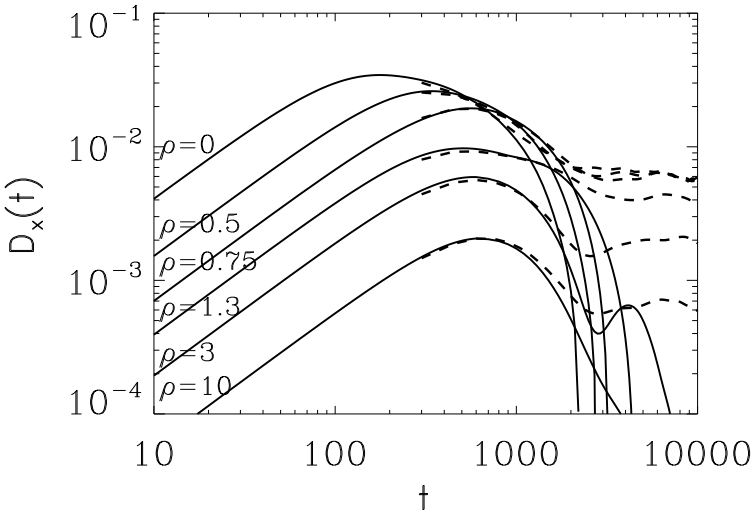

FIG. 11: $D_x(t)$ for a poloidally drifting potential with $v_{\rm dr} = 0.0013$. Solid lines: static potential ($K = \infty$); dashed lines: time-dependent potential ($K = 18$). According to the estimate $\tau_{\rm drop} \approx 2\lambda_c/v_{\rm dr}$, we find $\tau_{\rm drop} \approx (1520, 1920, 2400, 2890, 2630)$ for $\rho = (0, 0.5, 0.75, 1.3, 3)$ and $K = \infty$. These values are in reasonable agreement with the $D_x(t)$ curves. For $K = 18$, we find saturation at $t \sim \tau_c \approx 3000$.

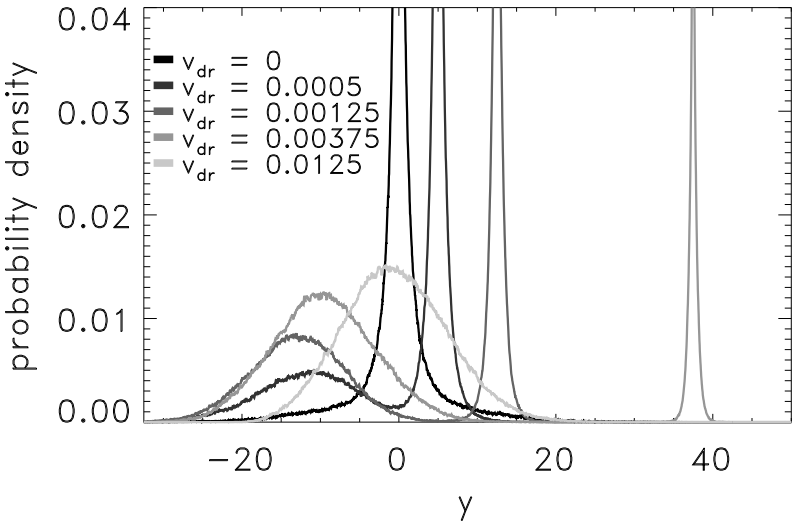

FIG. 12: PDF of the particle displacements in the y direction in a static, drifting potential (for different values of $v_{\rm dr}$) at $t = 10000$. The number of trapped particles (moving to the right) decreases as $v_{\rm dr}$ increases, and the average position of the untrapped particles (mostly moving to the left) is approximately constant for $v_{\rm dr} < V = 0.0053$ but decreases rapidly for $v_{\rm dr} > V$. Note that the right maximum for $v_{\rm dr} = 0.0125$ is outside the range of the figure.

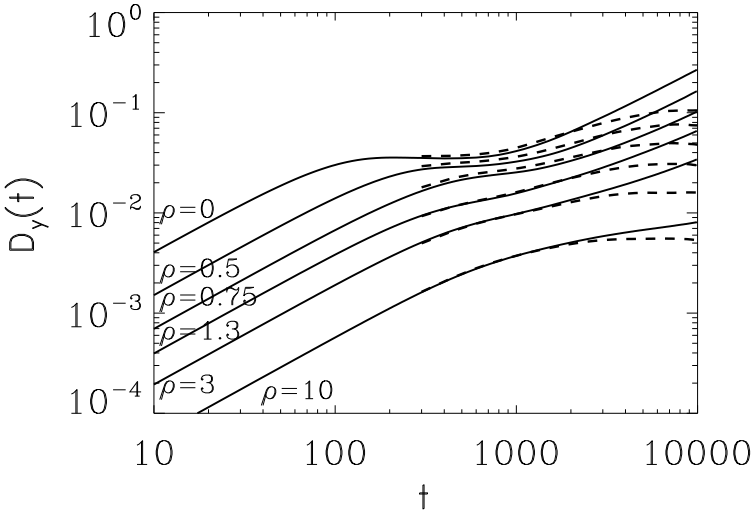

FIG. 13: Same as Fig. 11, but for the y direction.

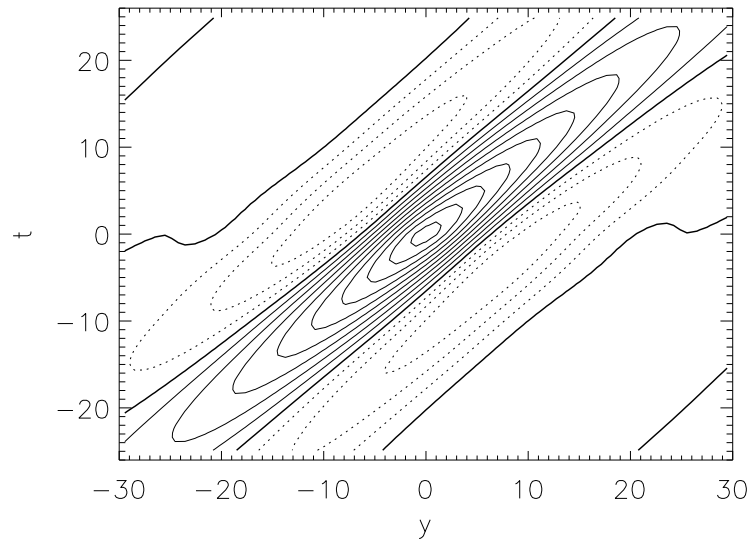

FIG. 14: Autocorrelation function $E(y,t)$ of the electrostatic potential obtained from a gyrokinetic simulation of trapped electron mode turbulence with the GENE code. Solid lines: positive values; dashed lines: negative values. The existence of a poloidal drift is evident.

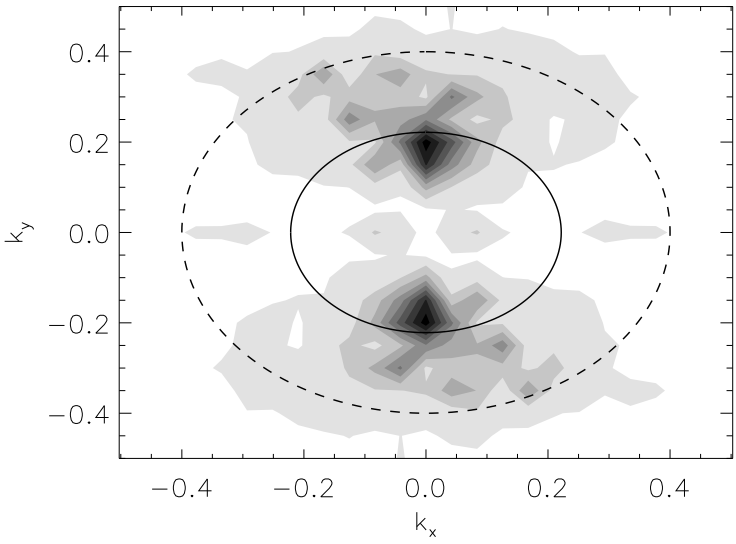

FIG. 15: Autocorrelation spectrum $E(k_x,k_y)$ of the potential from Fig. 14. The solid and dashed lines denote, respectively, the points where the squared Bessel function $J_0^2(k\rho)$ drops to $1/e$ times its maximum value and where it has its first zero. Here, $\rho = 6$, for which value both correlation lengths reach their maximum.

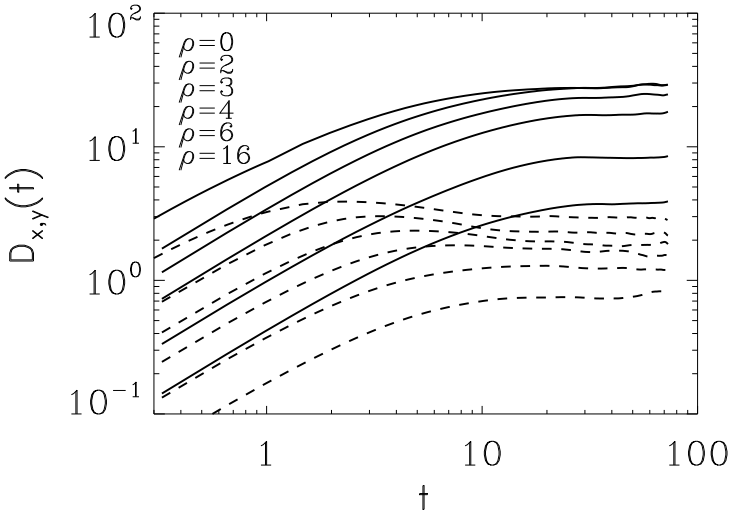

FIG. 16: $D_x(t)$ (solid lines) and $D_y(t)$ (dashed lines) for the potential of Figs. 14 and 15 – but without poloidal drift – for different gyroradii. The Kubo number is $K = 8.6$ and the correlation time/lengths are $\tau_c = 15$, $\lambda_x = 6.1$, and $\lambda_x = 4.2$. The parameters in the legend correspond to the order of the curves.

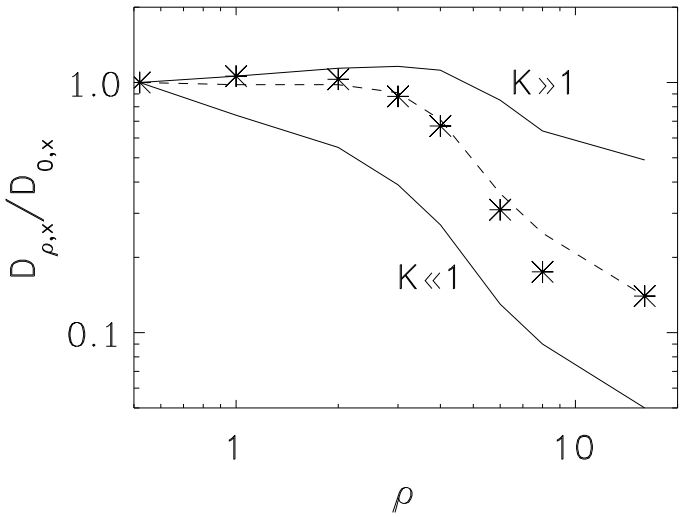

FIG. 17: Comparison between the simulation results (symbols) for the potential from Fig. 16 and the semi-analytical approach described in Secs. II and III (solid lines) for $K \ll 1$ and $K \gg 1$. The subscripts ρ and 0 denote, respectively, cases with finite and vanishing gyroradius. The dashed curve is an extension of the usual semi-analytical approach, employing a "dynamical" $\gamma(\rho)$.

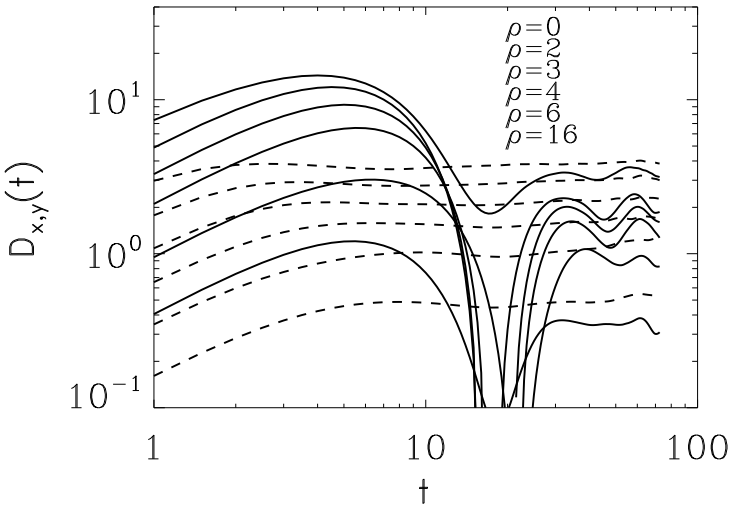

FIG. 18: Same as Fig. 16, but including the poloidal drift.